Structural and photoelectric properties of tensile strained $BiFeO_3$

Jonathan J. P. Peters, Alan E. Brunier, Affan N. Iqbal, Marin Alexe, and Ana M. Sanchez

University of Warwick, Coventry, CV4 7AL, United Kingdom

(Dated: June 4, 2020)

Abstract

An in-depth structural study of a 23 nm thick $BiFeO_3$ film grown on orthorhombic $NdScO_3$ $(110)_O$ substrates demonstrates the presence of a mixed phases. Atomic resolution scanning transmission electron microscopy measurements reveal an out-of-plane stripe domain structure typical of rhombohedral $BiFeO_3$ films but with a polarisation component along pseudocubic $\langle 100 \rangle_{PC}$ or canted from the $\langle 111 \rangle_{PC}$ towards the in-plane direction. Photovoltaic measurements display an anomalous modulation of the open circuit voltage as temperature is decreased that is attributed to a structural change associated with a transition to a single structural phase.

I. INTRODUCTION

Strain engineering is a critical component of thin film growth of functional oxide materials, frequently being used to stabilise ferroelectric polarisation or tune functional properties [1–3]. $BiFeO_3$ (BFO) is a material of particular interest for strain engineering because of its rich strain-temperature phase diagram and its multiferroicity, being ferroelastic, ferroelectric and antiferromagnetic at room temperature [4]. This opens up the possibility to manipulate one order parameter via control of another (e.g. controlling magnetisation through ferroelectric switching) [5, 6]. Furthermore, BFO exhibits an anomalous photovoltaic effect, whith a large open circuit voltage exceeding the band gap [7–9], showing promise for solar cell or photodetector applications. As such, epitaxial BFO has been under the spotlight with a wealth of theoretical and experimental research available in the literature. However, the behaviour of BFO under tensile strain is relatively poorly understood. As the photovoltaic effect is expected to be dependent on the material's structure [10, 11] and it has been demonstrated that compressive strained BFO grown on $LaAlO_3$ (LAO) produces a persistent photoconductivity [12], tensile strained BFO could provide further enhancement or control of the photovoltaic properties.

At room temperature, bulk BFO is a pseudo-cubic (PC) perovskite structure with the $R3c$ space group (lattice parameters $a = 3.965$ Å, $\alpha = 89.4°$). Under compressive strain, a tetragonal phase is formed with intermediary monoclinic M_A or M_C phases (in the notation of Vanderbilt and Cohen [13]) as well as mixed monoclinic phases possible, see Fig. 1 [14]. Under tensile strain, ranging from 2-7 % [15–18], first principles and thermodynamic calculations have predicted that an orthorhombic (O) phase of BFO can be stabilised as well as an equivalent monoclinic intermediary phase, M_B, as shown in Fig. 1. At the strain-induced phase boundary between rhombohedral-like monoclinic M_B (space group Cc or Cm) and orthorhombic, dielectric and piezoelectric properties are expected to be significantly enhanced [17].

Experimentally, a number of structural phases of BFO under tensile strain have been reported. These include monoclinic M_B [19, 20], orthorhombic [21, 22], mixed orthorhombic-rhombohedral [23, 24] and even tetragonal [25]. Considered together, these do not provide a coherent picture. For example Yang et al. [21] stabilised a purely orthorhombic BFO phase on $NdScO_3$ (NSO) ($Pbnm$ space group, mismatch +0.9%) with purely in-plane polarisation. Similar growths on $PrScO_3$ (mismatch +1.5%) substrates, expected to favour orthorhombic BFO even more due to its higher tensile strain, produced a single phase monoclinic M_B [19]. Therefore it seems that considerations other than strain (e.g. growth method/rate, doping) are integral to the structural phase formed. This was found to be the case for BFO grown on $LaAlO_3$ where compressive strain stabilises a tetragonally distorted phase and rhombohedral-tetragonal mixed phase regions may exist [26]. To add to the complexity, it has been demonstrated that, even in effectively unstrained BFO films grown on $TbScO_3$, bound charges at domain walls can induce tetragonal-like structures and nanodomains with unconventional domain walls [27].

Here, we report a detailed characterisation of the structure of BFO films grown on NSO, showing a mixed phase. Using atomic resolution transmission electron microscopy (TEM), the polarisation and domain structure of this mixed phase are explored. We then further investigate the functional properties of this system and demonstrate an unconventional photovoltaic response compared to typical single phase BFO thin films with stripe domains [9].

II. EXPERIMENTAL METHODS

BFO films were grown on NSO $(110)_O$ substrates (where the subscript O indicates indexing in the orthorhombic setting, as opposed to the pseudocubic, PC, setting) by pulsed laser deposition using a target with nominal 5 % Bi excess. A growth temperature of 640 °C in an oxygen environment of 0.2 mbarwas used. The laser fluence was $\sim$ 0.5 J cm^{-2} with a spot size of 9 mm^2, target substrate distance was 45 mm and pulse frequency was 8 Hz. The growth rate was approximately 0.38 Å s^{-1}. After deposition, the sample was cooled at a rate of 20 °C per minute at an oxygen pressure of 5 mbar.

High resolution X-ray diffraction (XRD) and reciprocal space mapping was performed using a Panalytical X'Pert Pro MRD diffractometer, using Cu K_α radiation and an X'Cellerator detector (Panalytical). SEM images were acquired on a Zeiss GeminiSEM 500 operating at 3 kV.

Detailed structural investigations were performed from scanning TEM (STEM) images acquired using a double aberration corrected JEOL ARM-200F - operating at 200 kV with a Schottky field emission source. Annular dark field (ADF) images were acquired using a collection angle of 45-180 mrad. TEM specimens were prepared with a JEOL JIB-4500 focussed ion beam using standard lift out procedures. For accurate position/displacement measurements, each image is an average of several fast scans, aligned for rigid and non-rigid distortions using the SmartAlign routines [28]. Atom positions where then found from local maxima and refined using non-linear least squares fitting of 2D Gaussian functions, including contributions from nearest neighbours.

For photovoltaic measurements, Au electrodes with widths of 700 μm, separated by 80 μm and with a nominal thickness of 50 nm were deposited by e-beam evaporation through a shadow mask. The sample was photoexcited with a 405 nm (3.07 eV) Newport LQA405-85E laser with a 55 $mWcm^{-2}$ intensity. The surface irradiation area (including electrodes) was 1.53 cm^2.

III. RESULTS AND DISCUSSION

Single BFO 00L peaks from XRD measurements, show in Fig. 2(a), reveal a constant out-of-plane pseudo-cubic lattice parameter of 3.89 ± 0.01 Å that is consistant with previous measurements of BFO under tensile strain of 3.90 Å [21] and 3.884 Å [19] (the unstrained bulk value is 3.965 Å [29]). Laue fringes are also observed, with a periodicity corresponding to a film thickness of 23 nm.

Due to the lack of a bottom electrode, conventional piezo force microscopy measurements of the polarisation and domains are not possible. Instead we use SEM measurements to image the domains, as demonstrated by Alyabyeva et al. [30]. Figure 2(b) shows an image demonstrating the domain structure, where a stripe domain structure can be seen with width of ~ 30 as well as a longer range bundles of domains. It is assumed, from comparison BFO with typical 71° domains [30, 31], that each bundle has the same out-of-plane polarisation component, but the stripes within correspond to varying in-plane polarisation. This differs from the purely orthorhombic BFO-NSO system demonstrated by Yang et al. [21] where the polarisation vector was purely in-plane.

Figure 3 shows reciprocal space maps (RSMs) for the 00L reflections. The main BFO and NSO peaks are both visible along the $q_{\|} = 0$ plane (at $q_{\perp} = 1.57$ Å^{-1} and $q_{\perp} = 1.61$ Å^{-1}, respectively, in the 001_{PC} case), showing the BFO is fully strained to the NSO, and there is no splitting in $q_{\perp}$, again indicating a single out-of-plane BFO lattice parameter of 3.885 ± 0.002 Å. A set of satellite peaks is visible at a fixed $q_{\|}$ in all 00L maps, corresponding to the 30 nm domain widths. In typical rhombohedral BFO, the spacing of these satellites is expected to increase with the diffraction order, corresponding to the rotation in the crystal lattice. This is demonstrated in Fig. 4 where the $q_{\|}$ positions of the 00L peaks has been plotted for the film examined here as well as a rhombohedral BFO film grown on $DyScO_3$. The data here are consistent with both the orthorhombic and the monoclinic M_B phases previously observed [19, 21].

For the 003 and 004 RSMs, slightly higher $q_{\|}$ and lower $q_{\perp}$ reflections are visible. The position of these peaks in the 004 reflection is ~ 10 % higher than for 003, indicating some rotation of the crystal lattice, though much weaker than for the fully rhombohedral film. These different peaks would suggest that there are in fact two similar phases, one more orthorhombic than the other.

To delve deeper into the true nature of the BFO structure, atomic resolution STEM imaging was performed as shown in Figs. 5(a) and 5(b). Here the initial structure can be observed. An atomically sharp NSO-BFO interface is observed and the film thickness is measured as ~ 23 nm (though some areas show a roughness with varying thickness from $18 - 25$ nm), in agreement with XRD measurements. Within the NSO, the 'zig-zag' of the A-lattice is observed, indicating that the NSO is viewed along a $\langle 110 \rangle_O$ direction of the $Pbnm$ structure (see supplementary material Fig. S1 [32]). It is important to note that this 'zig-zag' structure is also the surface structure that the BFO is grown on (i.e. $[110]_O$ and $[1\bar{1}0]_O$, or

$[100]_{PC}$ and $[010]_{PC}$, are equivalent in the unit cell of Fig. 1(b)).

The BFO also appears to show its characteristic polar displacement between the A-site and B-site lattices along $\langle 111 \rangle_{PC}$. However, STEM images show a projection of the structure, so it is not possible to determine if a displacement out of the image plane is present, as would be consistent with a rhombohedral structure, or not, as with orthorhombic. Nevertheless, the component of the displacement in the image-plane can be measured and mapped, as shown in Figs. 5(c) and 5(d). Here, several domains within the film are clearly present, some of which have been highlighted in Figs. 5(e)-(g) (The domain structure over a larger area is shown in Fig. S2 the supplementary materials [32]). Again these domains resemble typical rhombohedral BFO domains (of type 71°, appearing as a 90° rotation in the projected image, or 109° and 180°, both appearing as 180° in the projection) instead of the purely in-plane domains of Yang et al. [21]. From here on, these domain walls will be referred to using the projected angle (i.e. 90° or 180°). The domains widths ($\sim$ 30 nm) also correlate well with the macroscopic measurements of Fig. 2 and Fig. 3. The domain walls are mainly atomically sharp, though single unit cell step kinks can be seen in both the 90° and 180° walls in Fig. 5(d) (also shown towards the top of Fig. 5(d), for both domains walls).

The exact direction of the polarisation can be seen in several places to differ from the 45° orientation, particularly in Fig. 5(f). Figure. 6 shows histograms of the polarisation vector angle (excluding the substrate) for both sets of domains in Figs. 5(a) and 5(b). The most striking observation from this plot is the face that the polarisation direction does not lie along the 45° (or equivalent) angles, instead favouring a more in-plane vector. For example, the 3 distinct polarisation directions are centred around $46.7 \pm 0.3°$, $149.3 \pm 0.6°$ and $216.9 \pm 0.8°$, the latter two being $\sim$ 15° and $\sim$ 10° off from the expected $\langle 111 \rangle_{PC}$ direction. The domain angled at 46.7° also has quite a large distribution (with a standard deviation of 17°, compared to 10° and 11° for the other domains) suggesting that there is a phase with with off-45° polarisation, most likely M_B from Fig. 1. In all cases, there is a non-negligible presence of polarisation purely in-plane or out-of-plane, most obviously closer to the surface or in the vicinity of both the NSO interface and the 180° domain, shown in Fig. 5(f). Such polarisation orientations are consistent with tetragonal or orthorhombic structure projections, though a tetragonal structure under tensile strain is unlikely. This suggests there is a complex strain relation here between the substrate strain, strain of the 180° domain wall and possibly even the 90° domain wall. Similar effects in similar domain wall configurations can be seen in rhombohedral BFO grown on $DyScO_3$ (DSO) [27]. Nevertheless, the polarisation angle distributions shown in Fig. 6 add further evidence to the presence of multiple similar phases.

So far we have examined the structure of BFO grown on NSO, but it is interesting to see how this structure translates to functional properties, particularly in comparison to conventional unstrained, rhombohedral BFO thin films. The photovoltaic effect was examined for the films analysed here, as shown in Fig. 7. Two device configurations are examined, one with the electrodes parallel to the domain wall (PLDW) and another with the electrodes perpendicular to the domain walls (PPDW) as show in Fig. 7(a). Figure 7(b) shows typical photocurrent-voltage curves for both device configurations at 300 K, where the y-intercept gives the short circuit current, I_{SC}, and the x-intercept gives the open circuit voltage, V_{OC}. These curves look very similar to data acquired for 109° stripe domains in BFO [9], with a large V_{OC} of 13.8 V for the PLDW configuration. Furthermore, the power conversion efficiency, calculated as 3.67×10^{-5}, is typical of other BFO systems [8].

I_{SC} and V_{OC} have been plotted as a function of temperature in Figs. 7(c) and 7(d), where I_{SC} has been converted to the photocurrent density, J_{ph}, using the BFO film cross-section area (23 nm $\times$ 700 μm). Figure. 7(e) then shows the calculated photoconductivity, σ_{ph}. The curves for the PPDW configuration look typical for BFO films, with a large photocurrent due to the conductive domain walls and lower V_{OC} compared to the PLDW configuration. The PLDW case looks similar to previous measurements until the sample is cooled to 200 K, where the start of a decline in the V_{OC} is observed and an elbow in the J_{ph} curve. To explore deeper, we must turn to theory. The open circuit voltage is described by

$$V_{OC} = \frac{J_{ph} L}{\sigma_{dark} + \sigma_{ph}} \tag{1}$$

where σ_{dark} is the dark conductivity and L is the distance between the electrodes [33]. The temperature dependence on V_{OC} can be determined from Eqn. 1, where we also apply several assumptions. Firstly we use the fact that σ_{dark} is at least 10^2 smaller than σ_{ph} and can be safely ignored. Secondly, it has been demonstrated that J_{ph} is essentially temperature independent so can be ignored from temperature effects [33]. Furthermore, we do not expect that large strain would influence the absorption of the used light as the photon energy of the latter (3.06 eV) is much higher than any band gap variation potentially influenced by the strain [16]. Finally, we use the fact that the device geometry is constant with temperature.

This yields

$$V_{OC}\left(T\right) \propto \frac{1}{\sigma_{ph}\left(T\right)} \tag{2}$$

as σ_{ph} is expected to monotonically depend on temperature, there is clearly some other effect to cause the maxima in V_{OC} at 200 K for the PLDW configuration.

A proposed mechanism for the drastic deviation of the photovoltaic effect, compared to rhombohedral BFO films [9], relies on the mixed phase nature of the film observed here. The short circuit current is dependent on the lifetime of the carriers (and therefore the recombination rate) that is strongly dependent on the crystal lattice [9, 34]. For example, in BFO-LAO systems the relaxation processes are significantly different for the tetragonal and mixed tetragonal-rhombohedral phases due to strain, symmetry breaking and built in electric fields at phase boundaries [10, 26]. In the sample here, the multiple phases exist as part of a strain mediated thermotropic phase boundary between the rhombohedral and orthorhombic phases [35]. As the temperature is reduced, the structure may collapse to a single phase, resulting in the change of the electronic properties and giving the photovoltaic measurements seen in Fig. 7. Another possible explanation could involve the flexophotovoltaic effect where strain gradients between tetragonal and rhombohedral phases produce both enhanced and inhibited photoconductance [36]. It could therefore be possible that strain gradients between the mixed phases in the BFO films examined here might play an important role.

IV. CONCLUSIONS

We have stabilised a mixed phase BFO film grown on NSO under tensile strain. Basic characterisation of the sample shows an out-of-plane domain structure resembling a typical rhombohedral film as grown under minimal strain. A more in depth analysis of the structure using RSM and atomic resolution TEM reveals an orthorhombic like structure alongside a monoclinic phase. In fact, it is possible that a phase similar to the one shown here has been previously observed and measured without being noticed. The structure observed here is a result of lying on or near a strain-induced phase boundary between the rhombohedral and orthorhombic phases, which could be exploited to design a specific structural make-up. Finally, we suggest that the collapse of the mixed phase at low temperatures results in the abnormal temperature dependence of the photovoltaic effect, providing another possible route to modulate and control the electronic properties of BFO.

ACKNOWLEDGEMENTS

This work was supported by EPSRC grant EP/P031544/1.

NOTES

The authors declare no competing financial interest. The dataset for this publication may be obtained from http://wrap.warwick.ac.uk/135399.

[1] Jonathan Hwang, Zhenxing Feng, Nenian Charles, Xiao Renshaw Wang, Dongkyu Lee, Kelsey A. Stoerzinger, Sokseiha Muy, Reshma R. Rao, Dongwook Lee, Ryan Jacobs, Dane Morgan, and Yang Shao-Horn. Tuning perovskite oxides by strain: Electronic structure, properties, and functions in (electro)catalysis and ferroelectricity. *Materials Today*, 2019.

[2] Linxing Zhang, Jun Chen, Longlong Fan, Oswaldo Diéguez, Jiangli Cao, Zhao Pan, Yilin Wang, Jinguo Wang, Moon Kim, Shiqing Deng, Jiaou Wang, Huanhua Wang, Jinxia Deng, Ranbo Yu, James F. Scott, and Xianran Xing. Giant polarization in super-tetragonal thin films through interphase strain. *Science*, 361(6401):494–497, 2018.

[3] C. M. Folkman, S. H. Baek, H. W. Jang, C. B. Eom, C. T. Nelson, X. Q. Pan, Y. L. Li, L. Q. Chen, A. Kumar, V. Gopalan, and S. K. Streiffer. Stripe domain structure in epitaxial (001) $BiFeO_3$ thin films on orthorhombic $TbScO_3$ substrate. *Applied Physics Letters*, 94(25):251911, 2009.

[4] Yi Wang, Chris Nelson, Alexander Melville, Benjamin Winchester, Shunli Shang, Zi-Kui Liu, Darrell G. Schlom, Xiaoqing Pan, and Long-Qing Chen. BiFeO 3 Domain Wall Energies and Structures: A Combined Experimental and Density Functional Theory + U Study. *Physical Review Letters*, 110(26), 2013.

[5] R. Ramesh and Nicola A. Spaldin. Multiferroics: progress and prospects in thin films. *Nature Materials*, 6(1):21–29, 2007.

[6] L. W. Martin and R. Ramesh. Multiferroic and magnetoelectric heterostructures. *Acta Materialia*, 60(6):2449–2470, 2012.

[7] S. Y. Yang, J. Seidel, S. J. Byrnes, P. Shafer, C.-H. Yang, M. D. Rossell, P. Yu, Y.-H. Chu, J. F. Scott, J. W. Ager, L. W. Martin, and R. Ramesh. Above-bandgap voltages from ferroelectric photovoltaic devices. *Nature Nanotechnology*, 5(2):143–147, 2010.

[8] Marin Alexe and Dietrich Hesse. Tip-enhanced photovoltaic effects in bismuth ferrite. *Nature Communications*, 2(1):1–5, 2011.

[9] Akash Bhatnagar, Ayan Roy Chaudhuri, Young Heon Kim, Dietrich Hesse, and Marin Alexe. Role of domain walls in the abnormal photovoltaic effect in $BiFeO_3$. *Nature Communications*, 4(1):1–8, 2013.

[10] Pan Li, Xianglei Dong, Yuqiang Gao, Lixia Ren, and Kexin Jin. Photocarrier transport and dynamics in mixed-phase $BiFeO_3$ films. *Optics Express*, 24(8):9119, 2016.

[11] Zhifeng Huang, Peilian Li, Zhen Fan, Hua Fan, Qiuyuan Luo, Chao Chen, Deyang Chen, Min Zeng, Minghui Qin, Zhang Zhang, Xubing Lu, Xingsen Gao, and Jun-Ming Liu. Thickness dependence of photoconductance in strained $BiFeO_3$ thin films with planar device geometry. *physica status solidi (RRL) - Rapid Research Letters*, 12(1):1700301, 2018.

[12] Akash Bhatnagar, Young Heon Kim, Dietrich Hesse, and Marin Alexe. Persistent photoconductivity in strained epitaxial $BiFeO_3$ thin films. *Nano Letters*, 14(9):5224–5228, 2014.

[13] David Vanderbilt and Morrel H. Cohen. Monoclinic and triclinic phases in higher-order Devonshire theory. *Physical Review B*, 63(9):094108, 2001.

[14] Yajuan Zhao, Zhigang Yin, Zhen Fu, Xingwang Zhang, Jingbin Zhu, Jinliang Wu, and Jingbi You. Enhanced piezoelectric response of the two-tetragonal-phase-coexisted $BiFeO_3$ epitaxial film. *Solid State Communications*, 252:68–72, 2017.

[15] Yurong Yang, Wei Ren, Massimiliano Stengel, X. H. Yan, and L. Bellaiche. Revisiting properties of ferroelectric and multiferroic thin films under tensile strain from first principles. *Physical Review Letters*, 109(5):057602, 2012.

[16] Zhen Fan, John Wang, Michael B. Sullivan, Alfred Huan, David J. Singh, and Khuong P. Ong. Structural instability of epitaxial (001) $BiFeO_3$ thin films under tensile strain. *Scientific Reports*, 4:4631, 2014.

[17] Y. Y. Liu, L. Yang, and J. Y. Li. Strain-engineered orthorhombic-rhombohedral phase boundary in epitaxial bismuth ferrite films. *Journal of Applied Physics*, 113(18):183524, 2013.

[18] B. Dupé, S. Prosandeev, G. Geneste, B. Dkhil, and L. Bellaiche. $BiFeO_3$ films under tensile epitaxial strain from first principles. *Physical Review Letters*, 106(23):237601, 2011.

[19] Zuhuang Chen, Yajun Qi, Lu You, Ping Yang, C. W. Huang, Junling Wang, Thirumany Sritharan, and Lang Chen. Large tensile-strain-induced monoclinic m_b phase in $BiFeO_3$ epitaxial thin films on a $PrScO_3$ substrate. *Physical Review B*, 88(5):054114, 2013.

[20] D. Sando, Yurong Yang, E. Bousquet, C. Carrétéro, V. Garcia, S. Fusil, D. Dolfi, A. Barthélémy, Ph. Ghosez, L. Bellaiche, and M. Bibes. Large elasto-optic effect and reversible electrochromism in multiferroic $BiFeO_3$. *Nature Communications*, 7:10718, 2016.

[21] J. C. Yang, Q. He, S. J. Suresha, C. Y. Kuo, C. Y. Peng, R. C. Haislmaier, M. A. Motyka, G. Sheng, C. Adamo, H. J. Lin, Z. Hu, L. Chang, L. H. Tjeng, E. Arenholz, N. J. Podraza, M. Bernhagen, R. Uecker, D. G. Schlom, V. Gopalan, L. Q. Chen, C. T. Chen, R. Ramesh, and Y. H. Chu. Orthorhombic $bifeo_3$. *Physical Review Letters*, 109(24):247606, 2012.

[22] J. C. Yang, C. H. Yeh, Y. T. Chen, S. C. Liao, R. Huang, H. J. Liu, C. C. Hung, S. H. Chen, S. L. Wu, C. H. Lai, Y. P. Chiu, P. W. Chiu, and Y. H. Chu. Conduction control at ferroic domain walls via external stimuli. *Nanoscale*, 6(18):10524–10529, 2014.

[23] Yooun Heo, Jin Hong Lee, Lin Xie, Xiaoqing Pan, Chan-Ho Yang, and Jan Seidel. Enhanced conductivity at orthorhombic–rhombohedral phase boundaries in $BiFeO_3$ thin films. *NPG Asia Materials*, 8(8):e297–e297, 2016.

[24] Wanrong Geng, Xiangwei Guo, Yinlian Zhu, Yunlong Tang, Yanpeng Feng, Minjie Zou, Yujia Wang, Mengjiao Han, Jinyuan Ma, Bo Wu, Wentao Hu, and Xiuliang Ma. Rhombohedral–orthorhombic ferroelectric morphotropic phase boundary associated with a polar vortex in $BiFeO_3$ films. *ACS Nano*, 12(11):11098–11105, 2018.

[25] D. Sando, Bin Xu, L. Bellaiche, and V. Nagarajan. A multiferroic on the brink: Uncovering the nuances of strain-induced transitions in $BiFeO_3$. *Applied Physics Reviews*, 3(1):011106, 2016.

[26] Anoop R. Damodaran, Sungki Lee, J. Karthik, Scott MacLaren, and Lane W. Martin. Temperature and thickness evolution and epitaxial breakdown in highly strained $BiFeO_3$ thin films. *Physical Review B*, 85(2), 2012.

[27] Linze Li, Peng Gao, Christopher T. Nelson, Jacob R. Jokisaari, Yi Zhang, Sung-Joo Kim, Alexander Melville, Carolina Adamo, Darrell G. Schlom, and Xiaoqing Pan. Atomic scale structure changes induced by charged domain walls in ferroelectric materials. *Nano Letters*, 13 (11):5218–5223, 2013.

[28] Lewys Jones, Hao Yang, Timothy J. Pennycook, Matthew S. J. Marshall, Sandra Van Aert, Nigel D. Browning, Martin R. Castell, and Peter D. Nellist. Smart Align—a new tool for robust non-rigid registration of scanning microscope data. *Advanced Structural and Chemical Imaging*, 1(1), 2015.

[29] F. Kubel and H. Schmid. Structure of a ferroelectric and ferroelastic monodomain crystal of the perovskite $BiFeO_3$. *Acta Crystallographica Section B Structural Science*, 46(6):698–702, 1990.

[30] N. Alyabyeva, A. Ouvrard, I. Lindfors-Vrejoiu, O. Ageev, and D. McGrouther. Back-scattered electron visualization of ferroelectric domains in a $BiFeO_3$ epitaxial film. *Applied Physics Letters*, 111(22):222901, 2017.

[31] Z. H. Chen, A. R. Damodaran, R. Xu, S. Lee, and L. W. Martin. Effect of "symmetry mismatch" on the domain structure of rhombohedral $BiFeO_3$ thin films. *Applied Physics Letters*, 104(18):182908, 2014.

[32] See Supplemental Material at –INSERT-URL– for detail of the $NdScO_3$ substrate structure and additional TEM measurements, including electron diffraction and dark field imaging.

[33] Vladimir M. Fridkin. *Photoferroelectrics*. Springer Series in Solid-State Sciences. Springer-Verlag, Berlin Heidelberg, 1979.

[34] Marin Alexe. Local mapping of generation and recombination lifetime in $BiFeO_3$ single crystals by scanning probe photoinduced transient spectroscopy. *Nano Letters*, 12(5):2193–2198, 2012.

[35] Tom T.A. Lummen, Yijia Gu, Jianjun Wang, Shiming Lei, Fei Xue, Amit Kumar, Andrew T. Barnes, Eftihia Barnes, Sava Denev, Alex Belianinov, Martin Holt, Anna N. Morozovska, Sergei V. Kalinin, Long-Qing Chen, and Venkatraman Gopalan. Thermotropic phase boundaries in classic ferroelectrics. *Nature Communications*, 5(1), 2014.

[36] Ming-Min Yang, Affan N. Iqbal, Jonathan J. P. Peters, Ana M. Sanchez, and Marin Alexe. Strain-gradient mediated local conduction in strained bismuth ferrite films. *Nature Communications*, 10(1), 2019.

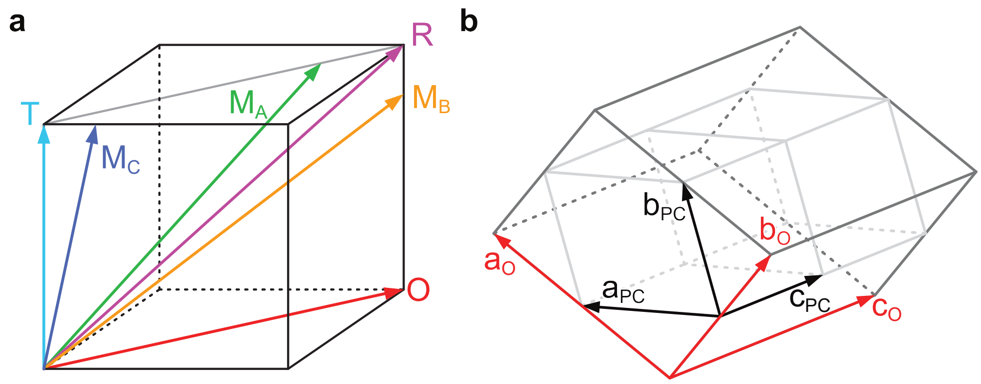

FIG. 1. (a) Schematic showing the relative polarisation direction for the tetragonal, T, rhombohedral, R, orthorhombic, O, and monoclinic, M, phases within the pseudocubic cell. (b) Relation between the substrate orthorhombic unit cell (given by vectors a_O, b_O and c_O) and the pseudocubic unit cell (vectors a_{PC}, b_{PC} and c_{PC}). The polar axis is then along $[100]_O$ or $[110]_{PC}$.

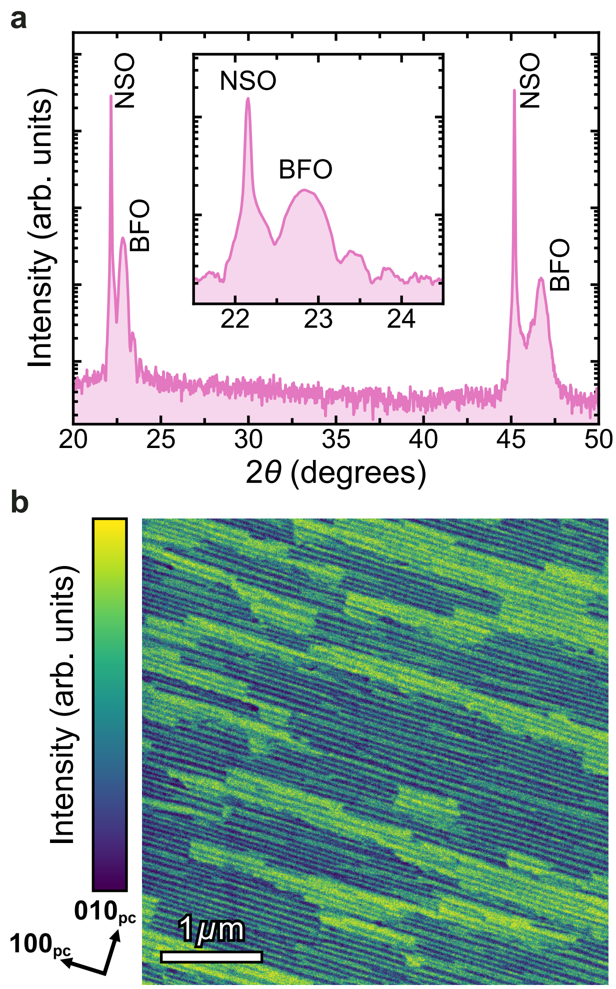

FIG. 2. (a) $\theta - 2\theta$ XRD scan of an as-grown BFO film in NSO showing the 001_{PC} (lower angles) and 002_{PC} (higher angles) reflections. Inset shows a zoomed in area of the 001_{PC} peaks. (b) Secondary electron SEM image showing contrast from the ferroelectric domains. 4 levels of contrast are visible, showing 4 domain types (2 in-plane components and 2 out-of-plane components).

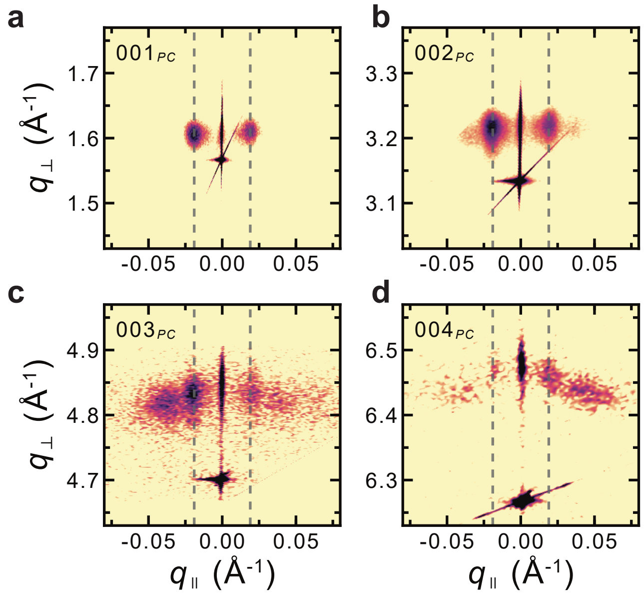

FIG. 3. Reciprocal space maps for the pseudo-cubic (a) 001, (b) 002, (c) 003 and (d) 004 reflections respectively. The position of the satellite peaks has been highlighted by the dashed lines.

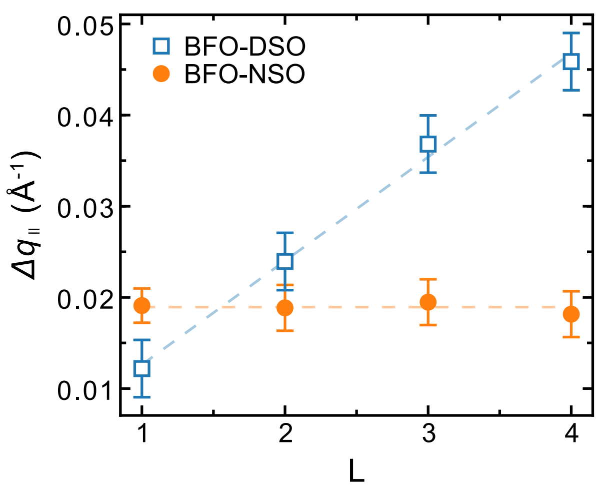

FIG. 4. Plot of the reciprocal space vector vs diffraction order L of the 00L reflections for fully rhombohedral BFO (BFO-DSO) and the BFO examined here (BFO-NSO). Measurements correspond to those shown in Fig. 3.

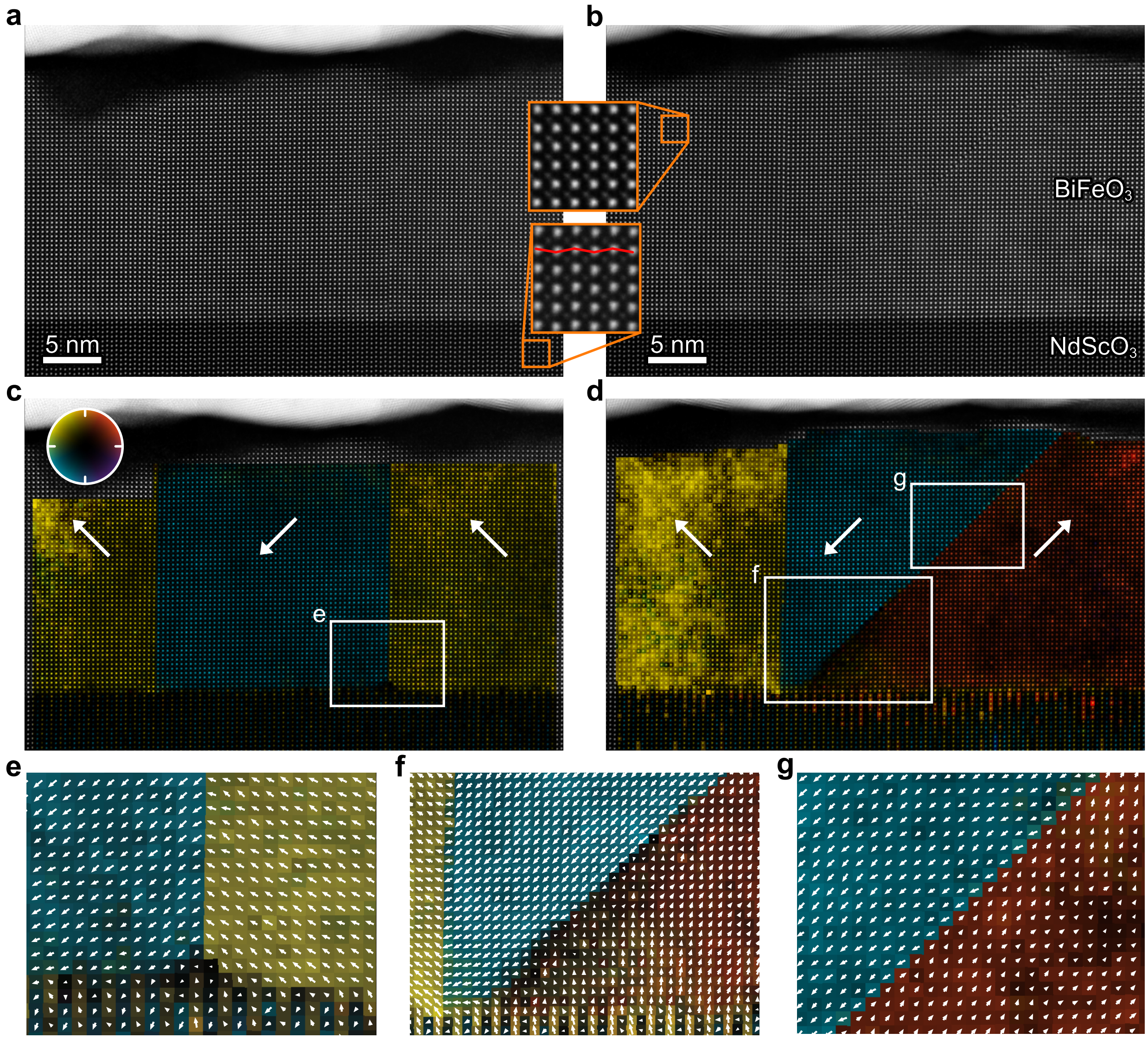

FIG. 5. (a) and (b) ADF images from two separate regions of the BFO film. Inset are magnified regions showing the BFO and NSO. (c) and (d) Displacement maps from (a) and (b), respectively, using the A-site movement with respect to the B-site lattice. Colour represents the displacement direction/magnitude given by the wheel inset in (c). (e)-(g) Magnified regions from (c) and (d) with the displacement vectors superimposed.

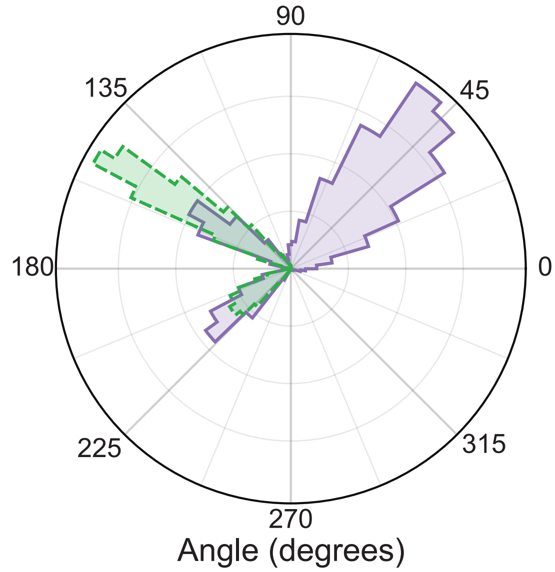

FIG. 6. Angle distribution of the Bi displacement with respect to the Fe lattice. The dashed green line corresponds to corresponds to Fig. 5(a) and solid purple line corresponds to Fig. 5(b).

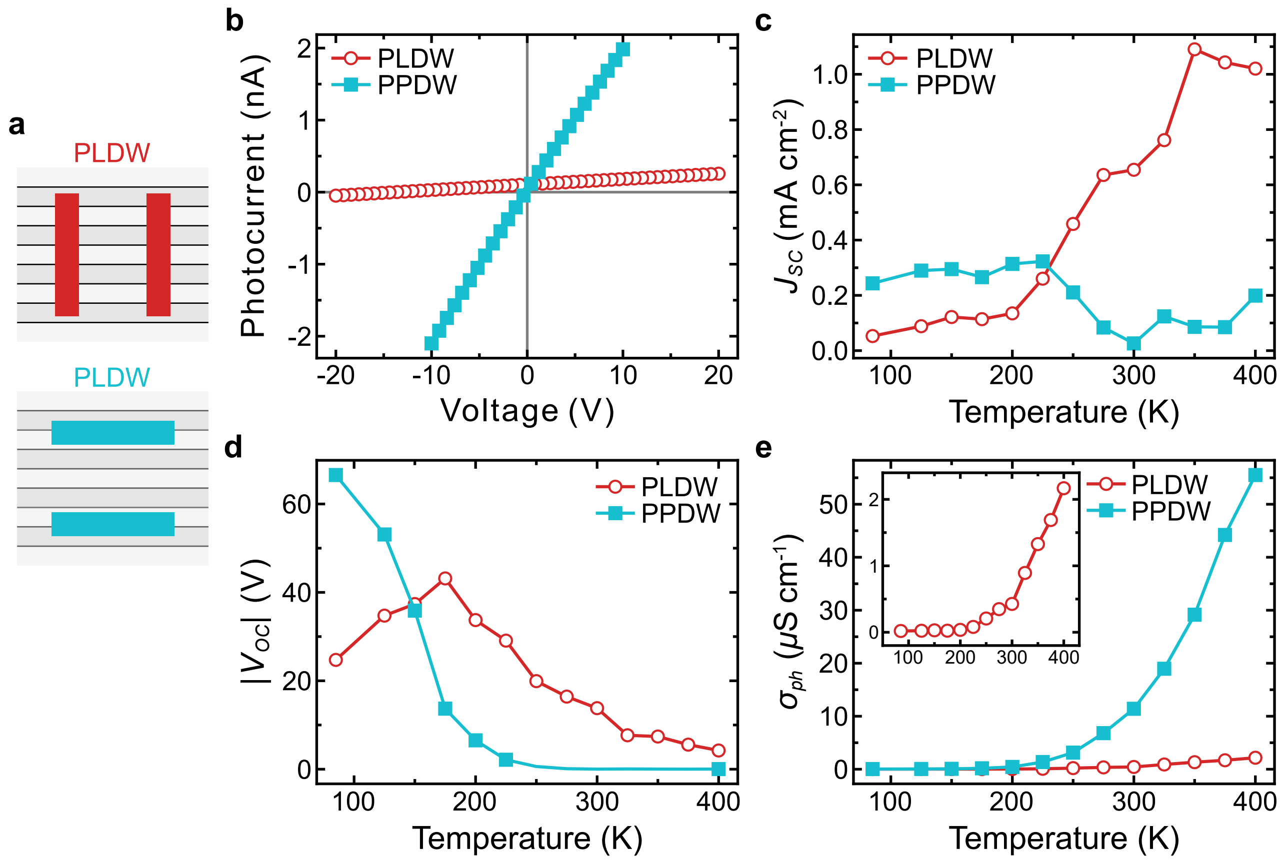

FIG. 7. (a) Measurement electrode configuration for electrodes parallel with the domain walls (PLDW) and perpendicular to domain walls (PPDW). (b) Photocurrent density behaviour for both configurations at 300 K. (c)-(e) Temperature dependence of the short circuit current density, open circuit voltage and photoconductivity, respectively. The inset in (e) shows the same PLDW data with the y axis scaled.